HAL
open science

Fluid Flux in Fractured Rock of the Alpine Fault Hanging-Wall Determined from Temperature Logs in the DFDP-2B Borehole, New Zealand

Lucie Janku-Capova, Rupert Sutherland, John Townend, Mai-Linh Doan, Cecile Massiot, Jamie Coussens, Bernard Celerier

To cite this version:

Lucie Janku-Capova, Rupert Sutherland, John Townend, Mai-Linh Doan, Cecile Massiot, et al.. Fluid Flux in Fractured Rock of the Alpine Fault Hanging-Wall Determined from Temperature Logs in the DFDP-2B Borehole, New Zealand. Geochemistry, Geophysics, Geosystems, 2018, 19 (8), pp.2631-2646. 10.1029/2017GC007317 . hal-01974319

HAL Id: hal-01974319

https://hal.science/hal-01974319v1

Submitted on 8 Jan 2019

HAL is a multi-disciplinary open access archive for the deposit and dissemination of scientific research documents, whether they are published or not. The documents may come from teaching and research institutions in France or abroad, or from public or private research centers.

L'archive ouverte pluridisciplinaire **HAL**, est destinée au dépôt et à la diffusion de documents scientifiques de niveau recherche, publiés ou non, émanant des établissements d'enseignement et de recherche français ou étrangers, des laboratoires publics ou privés.

Geochemistry, Geophysics, Geosystems

RESEARCH ARTICLE
10.1029/2017GC007317

Key Points:
- We use discrete wavelets to quantify anomalies in temperature logs that were measured during breaks in drilling
- Radial thermal gradients induced by borehole cooling, combined with fluid flux in adjacent rock, cause persistent temperature anomalies
- Fluid fluxes in zones of fractured rock are of order 10^{-6} m s^{-1}, and are 2–3 orders of magnitude higher than the regional flux

Supporting Information:
- Supporting Information S1
- Data Set S1
- Data Set S2
- Data Set S3
- Data Set S4
- Video S1
- Video S2

Correspondence to:
L. Janku-Capova,
lucie.capova@vuw.ac.nz;
R. Sutherland,
rupert.sutherland@vuw.ac.nz

Citation:
Janku-Capova, L., Sutherland, R., Townend, J., Doan, M.-L., Massiot, C., Coussens, J., & Celerier, B. (2018). Fluid flux in fractured rock of the Alpine Fault hanging-wall determined from temperature logs in the DFDP-2B borehole, New Zealand. *Geochemistry, Geophysics, Geosystems*, *19*, 2631–2646. https://doi.org/10.1029/2017GC007317

Received 1 NOV 2017
Accepted 5 MAY 2018
Accepted article online 12 MAY 2018
Published online 18 AUG 2018

© 2018. American Geophysical Union. All Rights Reserved.

Fluid Flux in Fractured Rock of the Alpine Fault Hanging-Wall Determined from Temperature Logs in the DFDP-2B Borehole, New Zealand

Lucie Janku-Capova[1], Rupert Sutherland[1], John Townend[1], Mai-Linh Doan[2], Cécile Massiot[3], Jamie Coussens[4], and Bernard Célérier[5]

[1]School of Geography, Environment and Earth Sciences, Victoria University of Wellington, PO Box 600, Wellington, New Zealand, [2]Univ. Grenoble Alpes, Univ. Savoie Mont Blanc, CNRS, IRD, IFSTTAR, ISTerre, 38000 Grenoble, France, [3]GNS Science, Lower Hutt, Wellington, New Zealand, [4]Ocean and Earth Science, National Oceanography Centre Southampton, University of Southampton, European Way, Southampton, SO14 3ZH, United Kingdom, [5]Géosciences Montpellier, Université de Montpellier, CNRS, Montpellier, France

Abstract Sixteen temperature logs were acquired during breaks in drilling of the 893 m-deep DFDP-2B borehole, which is in the Alpine Fault hanging-wall. The logs record various states of temperature recovery after thermal disturbances induced by mud circulation. The long-wavelength temperature signal in each log was estimated using a sixth-order polynomial, and residual (reduced) temperature logs were analyzed by fitting discrete template wavelets defined by depth, amplitude, and width parameters. Almost two hundred wavelets are correlated between multiple logs. Anomalies generally have amplitudes <1°C, and downhole widths <20 m. The largest amplitudes are found in the first day after mud circulation stops, but many anomalies persist with similar amplitude for up to 15 days. Our models show that thermal and hydraulic diffusive processes are dominant during the first few days of re-equilibration after mud circulation stops, and fluid advection of heat in the surrounding rock produces temperature anomalies that may persist for several weeks. Models indicate that the fluid flux normal to the borehole within fractured zones is of order 10^{-7} to 10^{-6} m s^{-1}, which is 2–3 orders of magnitude higher than the regional flux. Our approach could be applied more widely to boreholes, as it uses the thermal re-equilibration phase to derive useful information about the surrounding rock mass and its fluid flow regime.

Plain Language Summary The Alpine Fault is surrounded by highly fractured rock that allows groundwater to flow between the mountains and valleys. This contributes to high temperatures and fluid pressures at shallow depths in the valleys. In this paper, we show that analysis and modelling of repeated temperature measurements in a single borehole in a valley can be used to estimate where fractured zones are and how much water is flowing through them. Our results indicate that individual zones have flow rates up to 1,000 times greater than the regional average, which is already much greater than in most other mountain ranges. Our analysis may also provide useful information for estimation of potential fluid production rates and hence the commercial value of geothermal resources.

1. Introduction

Temperature influences physical properties (rheology, density, electrical conductivity, seismic velocity, fluid viscosity, etc.) and chemistry (phase changes, mineral formation, etc.), and temperature deviation from a linear geotherm in an environment without heat sources reflects fluid flow (Kappelmeyer & Haenel, 1974). Fluids play a fundamental role in the seismic cycle of active fault zones (Hickman et al., 1995). Temperature anomalies in a borehole may be the manifestation of fluid flow through permeable fractures (Vidal et al., 2016), disturbance of the thermal and hydrogeological regime of the rock mass by drilling (Lachenbruch & Brewer, 1959), or may represent zones governed by different thermal properties or processes of heat transfer (Clauser et al., 1997). In this paper, we document and describe temperature log data acquired in the DFDP-2B borehole during breaks in drilling, and show how persistent anomalies can be identified and quantified, and used to model zones of fluid movement through fractured rock of the Alpine Fault hanging-wall.

The main objective of the Deep Fault Drilling Project (DFDP) is to study conditions at depth adjacent to the Alpine Fault, which is an active plate boundary fault that is late in its typical earthquake cycle (Townend et al., 2009). The 893 m-deep DFDP-2B borehole yielded unexpectedly high temperatures for a plate-bounding fault in a nonvolcanic environment. It had an equilibrated bottom-hole temperature of 111°C and a mean geothermal gradient of 125°C/km (Sutherland et al., 2017). High permeability associated with the fractured rock has resulted in an active hydrogeological system in the Alpine Fault's hanging-wall (Sutherland et al., 2017; Townend et al., 2017; Upton & Sutherland, 2014). We use a discrete wavelet method to identify persistent anomalies in temperature logs that were measured at various times during postdrilling equilibration. We consider alternate models for the origin of these anomalies and show that they can be used to estimate fluid fluxes within localized fractured zones.

1.1. Equilibrium and Transient Temperatures After Drilling

Temperature logs are a cost-effective and widely employed tool for studying fluid flow in boreholes (Drury & Jessop, 1982; Ge, 1998; Kappelmeyer & Haenel, 1974; Michalski, 1989; Reiter, 2001). This is why they are commonly used for identification and analysis of permeable zones in scientific drilling projects (Clauser et al., 1997; Jobmann & Clauser, 1994; Kohl & Rybach, 1996; Popov et al., 1999; Vidal et al., 2016). In a homogeneous conductive environment with no heat sources, equilibrium temperature increases linearly with depth in accordance with Fourier's law of heat conduction (equation (1)),

$$\vec{q} = -\lambda \frac{dT}{dz} \tag{1}$$

where $\vec{q}$ is the vector of heat flux, $\frac{dT}{dz}$ is the temperature gradient in vertical direction, and λ is thermal conductivity. Deviations from this linear trend are often attributed to advection of heat by fluids (Saar, 2011), in which case a convex or concave shape of the temperature profile suggests downward or upward flow, respectively, and a local deviation from the trend suggests lateral flow (Bredehoeft & Papaopulos, 1965; Ziagos & Blackwell, 1986). In crystalline rocks with low intrinsic permeability, only some fractures may be permeable enough to allow sufficient flow to produce a temperature anomaly (Barton et al., 1995).

The process of drilling and mud circulation causes transient disturbance of the formation temperature field (Kappelmeyer & Haenel, 1974). In deep boreholes, drilling mud is colder than the rock environment at depth, but transfers heat upward as it is circulated back to the surface. Hence, the temperature profile shortly after drilling has a relatively low thermal gradient: temperatures are transiently raised in upper portions of the hole, and lessened in deeper portions. After mud circulation stops, the temperature profile equilibrates over time toward the background temperature distribution in the surrounding rock mass. The background temperature and drilling-induced changes are sensitive to fractures adjacent to the borehole. Drury and Jessop (1982) and Drury et al. (1984) described four main types of fractures and discussed their characteristic thermal signatures, based on observations in two example boreholes from the Canadian Shield. Type 1 fractures are not permeable before drilling, but become permeable and may communicate through the borehole, causing upward or downward flow. Type 2 fractures are permeable only while pressurized by mud circulation, and leave characteristic thermal anomalies that decay with time. Type 3 fractures are naturally permeable before, during and after drilling. Drury (1989) describes their thermal signature to be similar to that of a change in thermal properties of the rock: a high thermal gradient above and low thermal gradient below is characteristic for type 3 fractures. Type 4 fractures are impermeable regardless of drilling operations. These may be detected by borehole imaging, but exhibit no thermal anomaly.

In the case of DFDP-2B, all operations used a bentonite mud system that was intended to block permeable fractures, so that fractured parts of the borehole wall (where mud losses occurred) were stabilized by a hydrated "filter cake" of bentonite and mud circulation could be maintained. Although fractured zones were largely stabilized by the mud system, some hydraulic communication with the rock mass remained, as evidenced by ongoing changes in surface mud level after circulation ceased (Townend et al., 2017). We consider the effects of type 2 and 3 fractures, but note that permeability in close proximity to the borehole wall was reduced by the mud system. We also consider the case when the mud system isolates the borehole hydraulically (but not thermally) from the formation, so that persistent moderate-amplitude thermal anomalies can be interpreted in terms of the flow of native groundwater in the surrounding formation.

1.2. Location and Geologic Setting

The Alpine Fault is a transpressional boundary between the Australian and Pacific plates in the South Island of New Zealand. It accommodates oblique dextral strike-slip motion at 23–27 mm/yr (Cox & Sutherland, 2007; Norris & Cooper, 2007; Sutherland et al., 2006) and uplift of 5–10 mm has produced the Southern Alps (Koons, 1987; Little et al., 2005; Norris & Cooper, 1997). GPS observations of regional interseismic vertical displacement indicate c. 5 mm/yr (Beavan et al., 2010), but local Quaternary uplift rates can be > 10 mm/yr (Norris & Cooper, 2001).

High precipitation on the western side of the Southern Alps contributes to extreme erosion that approximately balances uplift (Adams, 1980). The combination of rapid uplift and erosion results in hot rocks from depth being carried close to the surface before they are able to cool (Allis & Shi, 1995; Koons, 1987; Little et al., 2005). High fracture permeability of the inboard side of the orogen and high topographic gradients (Upton et al., 1995; Upton & Sutherland, 2014) allow infiltration of meteoric waters to depths of 6–8 km (Menzies et al., 2014; Upton et al., 1995). Extremely low permeability of the fault core forms a barrier to downward fluid flow (Menzies et al., 2014; Sutherland et al., 2012), resulting in fluid flow paths that advect heat into valleys such as the Whataroa Valley (Sutherland et al., 2017). The DFDP-2B borehole (Figure 1) was drilled through 240 m of glaciofluvial Quaternary sediments and into crystalline basement. Basement rock included a downhole progression from amphibolite-facies Torlesse Terrane Alpine Schist to protomylonite and mylonite of the Alpine Fault (Cox & Sutherland, 2007; Sutherland et al., 2015; Toy et al., 2015, 2017). The drilling technology that was used, combined with high mechanical anisotropy associated with moderately southeast-dipping foliation, resulted in a borehole tilt that increases downhole to a maximum value of 44° (Sutherland et al., 2015; Townend et al., 2017). All depths in this paper are measured drilled depth (MD), which differs from true vertical depth (TVD) as a result of the borehole's deviation from vertical (Sutherland et al., 2017; Townend et al., 2017).

2. Data

2.1. Temperature Data

Temperature logs in DFDP-2B were acquired in an open hole at different times after episodes of drilling and mud circulation to various depths during four phases of drilling (Table 1 and Figure 2). The logs provide a record of temperature recovery in the borehole after drilling. A permanent observatory with fiber-optic cable was installed in the borehole and distributed temperature sensing has since been used to monitor long-term thermal re-equilibration of the site (Sutherland et al., 2015, 2017).

Prior to the temperature logs presented here being acquired, the upper portion of the borehole was cased with steel casing to a depth of 264.93 m (Sutherland et al., 2015). Only the open-hole sections of logs are presented in this paper. During the first three phases of drilling, logs were run at 4 m/min. The ALT temperature and fluid conductivity logging tool (QL40-FTC) is rated to 70°C and the temperature sensor saturates at ~98°C, so measurements in the deeper (hotter) portions of the hole during phase IV had to be acquired quickly (at a logging speed of 10–15 m/min). All logs were subsequently depth-matched using the stacked natural gamma tool (Remaud, 2015). For technological details of the tools, stacks and acquisition, see Sutherland et al. (2015).

The initial logging sessions (phase I) were conducted when the borehole was 397 m deep: they encompassed runs 04–25 with a brief interval of mud circulation before run 16. Logging runs 27–35 (phase II) were measured after drilling progressed to 490 m. Runs 36–44 (phase III) were measured when the drilled depth had reached 547 m. The last two runs (phase IV), run 45 and the three passes of run 49, were measured after drilling to 815 and 893 m, respectively. Due to the high temperatures encountered, run 49 was logged in two separate passes (P1 and P2) on the way down, and was run at different speeds to minimize the time the tool spent in the hot environment. The remaining portion of the borehole was measured during the tool's ascent (P3). The curves of R49 are smoother than the curve of R45 because of minor flow disturbance in the static mud induced by the relatively fast-moving tool.

2.2. Hydraulic Observations

Drilling mud level and density control the fluid pressure balance between the hole and rock formation, and mud properties and levels were closely monitored during the course of the drilling (Figure 3) (Sutherland

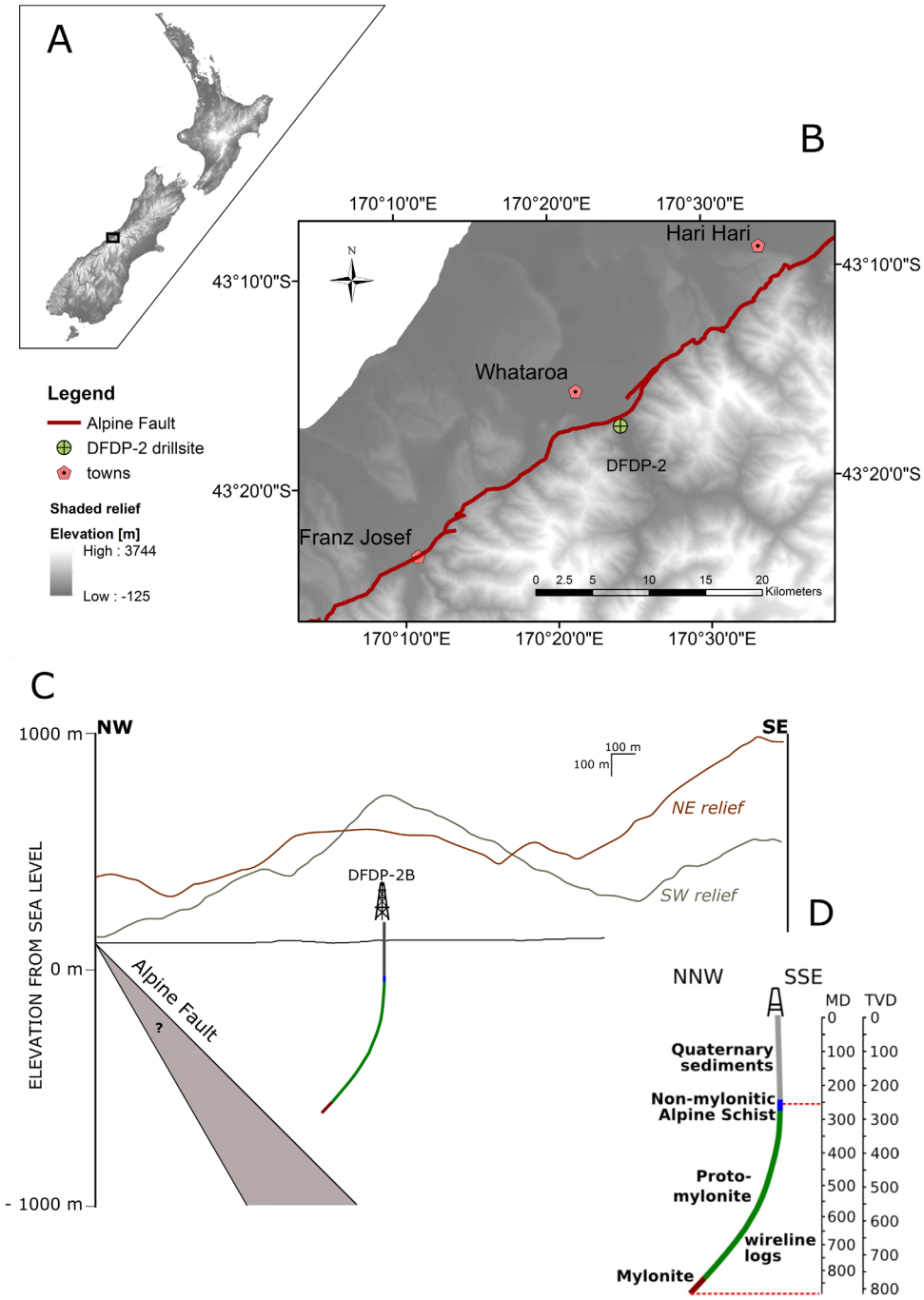

Figure 1. Location of the DFDP-2B borehole (a) in the context of New Zealand, and (b) in the context of Whataroa Valley and its surroundings. (c) Relative geometries of the borehole, Alpine Fault, and topography around Whataroa Valley. (d) Lithological profile of DFDP-2B. Figures 1c and 1d modified after Massiot (2015). MD refers to measured drilled depth, TVD refers to true vertical depth of the borehole.

et al., 2015). Within the borehole, we assume a linear vertical pressure gradient computed from the measured mud density and surface level. Drilling mud density was adjusted during drilling to maintain a pressure in the borehole equal to or slightly higher than formation pressure, to avoid mud dilution and uncontrolled borehole flow from the formation. Several minor mud losses associated with injection into the formation were identified during drilling (Coussens, 2017; Townend et al., 2017), but circulation was

Table 1
All Acquired Temperature Logs Together With the Time After the End of Circulation in the Hole When the Measurement Was Commenced, and the Depth Range at Which It Was Acquired

Name of log	Start of log (date yyyy/mm/dd, time hh:mm)	Time elapsed since end of circulation (h)	End of log (date yyyy/mm/dd, time hh:mm)	Depth from (m)	Depth to (m)
Temp_R04_P1	2014/10/23, 15:44	7.32	2014/10/23, 18:10	Top	396.82
Temp_R10_P1	2014/10/30, 19:10	178.75	2014/10/30, 20:37	Top	321.95
Temp_R16_P1	2014/11/5, 21:30	3.27	2014/11/5, 23:43	Top	394.25
Temp_R25_P1	2014/11/7, 05:50	35.6	2014/11/7, 07:08	264.2	390
Temp_R27_P1	2014/11/12, 12:20	10.4	2014/11/12, 14:35	Top	458.2
Temp_R29_P1	2014/11/13, 13:57	36.02	2014/11/13, 15:54	Top	489.32
Temp_R35_P1	2014/11/15, 05:00	75.07	2014/11/15, 07:35	Top	488.97
Temp_R36_P1	2014/11/18, 07:50	6.72	2014/11/18, 09:53	206.41	523.96
Temp_R38_P1	2014/11/19, 13:37	5.7	2014/11/19, 14:50	260.12	546.02
Temp_R42_P1	2014/11/19, 22:47	14.87	2014/11/20, 00:13	264.13	545.98
Temp_R43_P1	2014/11/24, 15:28	127.55	2014/11/24, 18:17	Top	523.47
Temp_R44_P1	2014/11/26, 10:00	170.08	2014/11/26, 12:17	Top	498.53
Temp_R45_P1	2014/12/4, 06:37	7.2	2014/12/4, 08:50	260.38	812.13
Temp_R49_P1	2014/12/9, 00:50	8.83	2014/12/9, 02:16	260.29	822.74
Temp_R49_P2	2014/12/9, 02:16	10	2014/12/9, 02:20	822.82	893.02
Temp_R49_P3	2014/12/9, 02:33	10.55	2014/12/9, 04:25	384.13	750.73

Note. "Top" refers to any depth <5 m. Note that the "Temp_R49_P3" log was acquired during the tool's ascent.

never lost completely and was fully re-established within tens of minutes. The expansion of bentonite particles in the mud due to hydration clogged these fractures and controlled losses of drilling fluids into the formation.

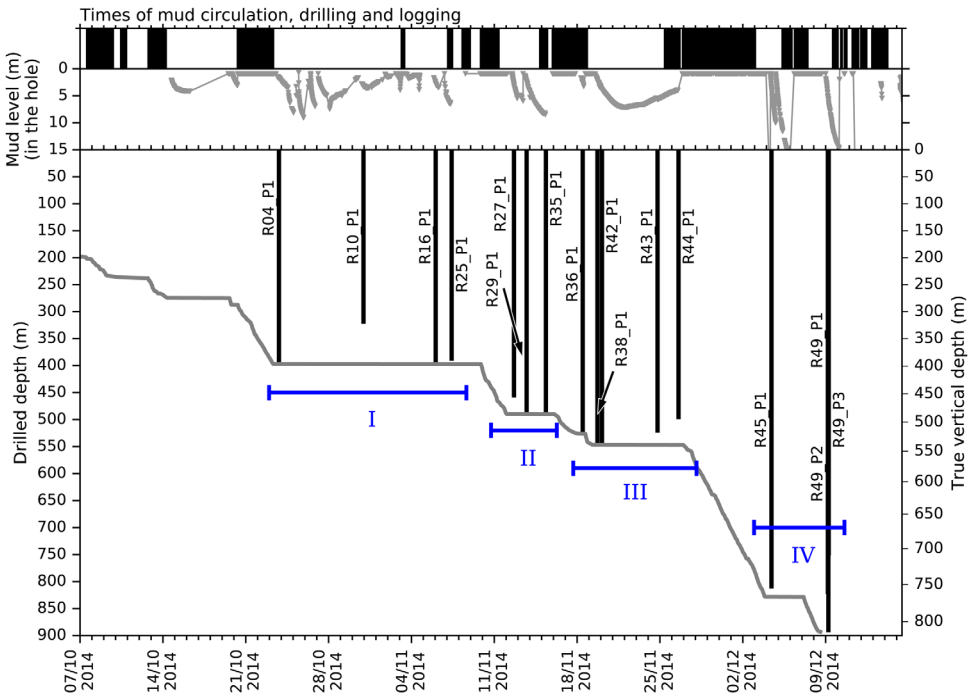

Figure 2. Drilling operations (drilled depth shown by a bold grey line), mud circulation (black bands represent times of mud circulation, white bands represent breaks in circulation), mud level changes in the borehole (grey triangles), and times when logging was taking place in the context of operations causing disturbance. Phases I–IV are marked for future reference. We use "R" (the term "run") to refer to the deployment in the borehole of a specific tool stack and "P" ("pass") to refer to a single record (see Appendix 7 of DFDP-2 Completion Report, Sutherland et al., 2015, for details.) Both the measured drilled depth (MD on the left) and true vertical depth (TVD on the right) are included for reference.

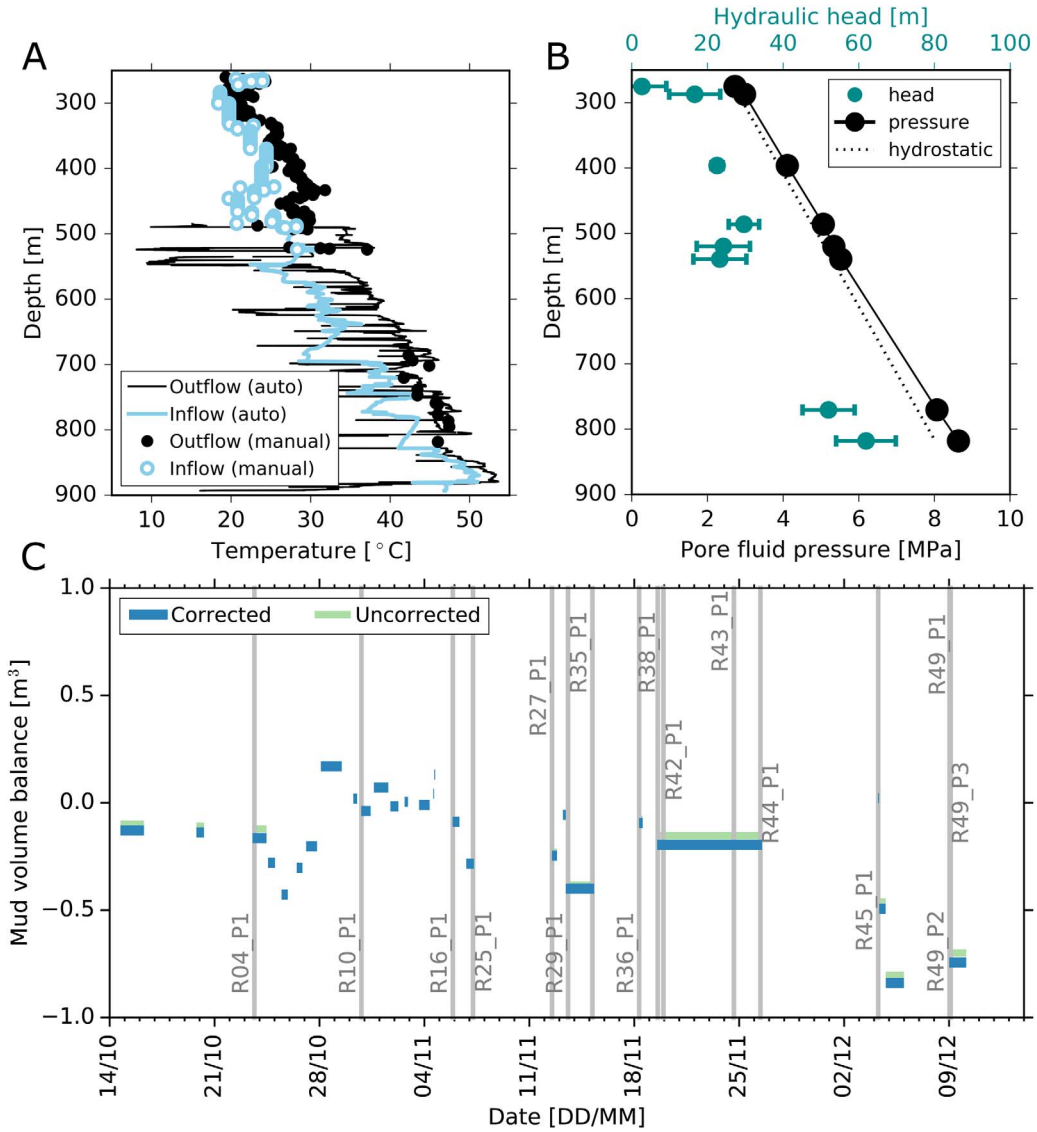

Figure 3. (a) Mud temperature during drilling (depth refers to the maximum drilled depth at the time of measurement). Discrete point measurements were taken manually by staff on site, automatic continuous measurements (solid lines) were acquired by sensors installed in the suction pit (Inflow) and in the outflow pipe (Outflow). (b) Pore fluid pressure from mud observations and hydraulic head (error bars showing the range within uncertainty) in the borehole (Sutherland et al., 2017). Hydrostatic pressure is plotted in dotted line for reference. (c) Total balance of mud (mud gained – mud injected) for each slug test corrected for maximum mud expansion at given temperature (thick blue line) and observed (thinner green line) (Coussens, 2017).

During breaks in drilling, mud particles settle on the bottom of the hole and thermal equilibration in the borehole leads to expansion of the drilling mud. These effects contributed to rises in mud level during Runs 10, 43, and 44 only negligibly (Figures 2 and 3).

3. Method

3.1. Isolation of Anomalies in Each Log

Detrending temperature data are a common practice to extract short-wavelength anomalies from temperature signal. We refer to the temperature logs after removal of a trend as "reduced temperatures." A distinctive temperature increase at the base of some logs (Figure 4) exists because the lower parts of the recently drilled hole underwent less disturbance and hence the temperature recovered more quickly. A linear trend,

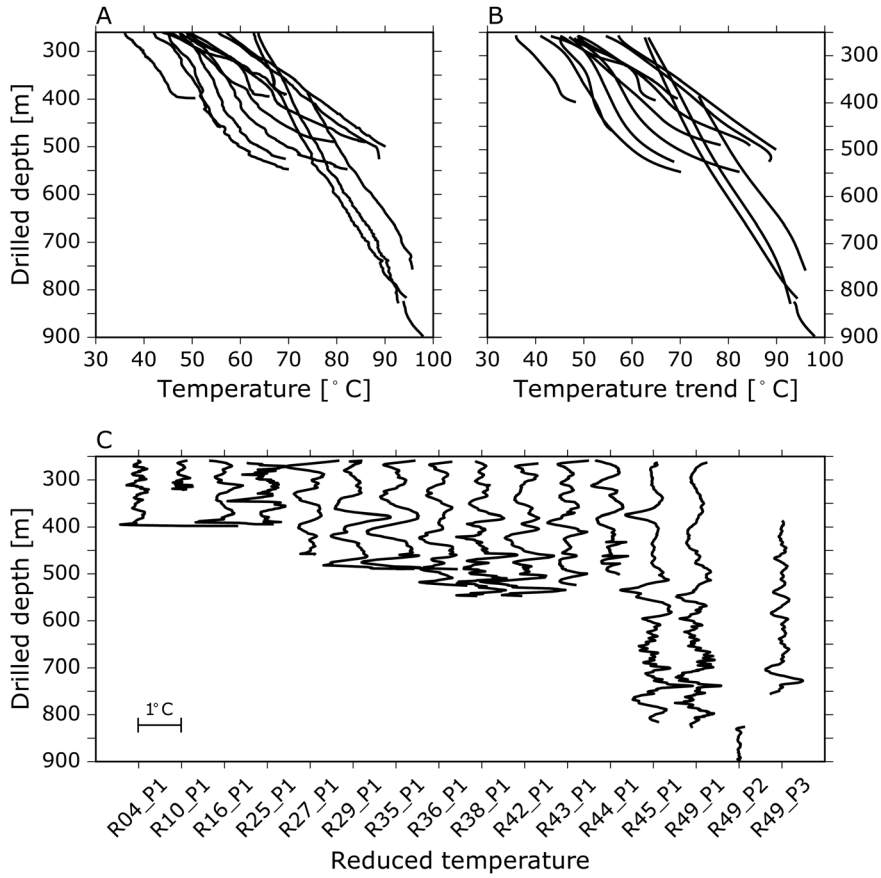

Figure 4. (a) All temperature logs as measured, (b) the long-wavelength portion of the signal approximated by a sixth-order polynomial, and (c) the reduced logs: A = B + C.

which is commonly used in constructing reduced temperature logs (Clauser et al., 1997), would not usefully remove the long-wavelength portion of signal as a result of this bottom-hole effect. Instead, we used a sixth-order polynomial. Figure 4 shows the original data, the polynomial approximations, and the reduced logs. Figure 5 illustrates how varying the order of the polynomial affects our estimation of the long-wavelength signal in the logs (referred to below as the "trend").

We use an objective method of quantitatively identifying and characterizing anomalies in the DFDP-2B reduced temperature logs. We fit a continuous template of discrete wavelets (Figure 6) with variable position (x_0), amplitude (A) and width parameter (w), by minimizing the sum of squares (equation (2)) for the log:

$$S=\sum_{i=0}^{N}(T_i-F_i)^2 \tag{2}$$

Here, T_i is reduced temperature and F_i is the wavelet function (Figure 6) at each corresponding depth in the log. Wavelets are iteratively searched for in the reduced temperature log. Each fitted wavelet is then subtracted from the log and the next search conducted.

We use a Gaussian wavelet (equation (3)), because it has a single peak and is hence unambiguous. The width parameter w is about 25% of the full spatial extent of the wavelet. However, there may be oscillations in reduced temperature associated with filtering, so we also consider two alternate wavelets: Ricker (equation (4)), where w is the distance between the positive and negative peaks; and Gaussian derivative (equation (5)), where w is the distance of either peak from the inflexion point (Figure 6).

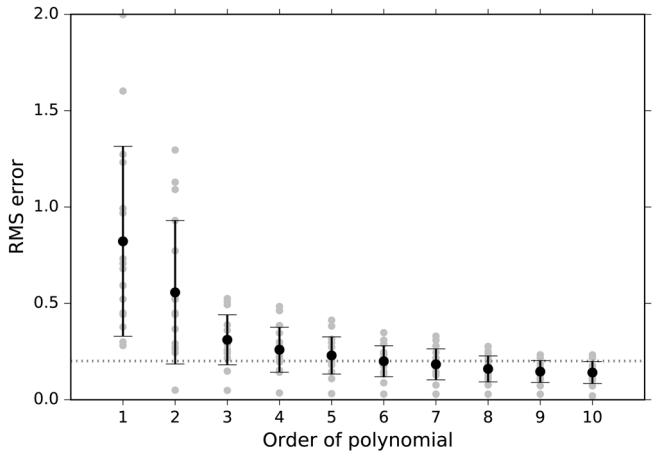

Figure 5. A RMS error between the measured data and the fitted polynomial for each log (grey dots) with changing order of the polynomial function. We chose a threshold for the mean RMS error (black dots with error bars representing the standard error of the mean) ≤ 0.2 (horizontal dotted line) to select the minimum order of polynomial that accurately represents the long-wavelength measured data without removing short-wavelength anomalies.

$$G(x, x_0, A, w) = Ae^{\frac{-(x-x_0)^2}{2w^2}} \tag{3}$$

$$R(x, x_0, A, w) = A\left(1 - \frac{\sqrt{x-x_0}}{\frac{w^2}{4}}\right)e^{\frac{\sqrt{x-x_0}}{w^2}} \tag{4}$$

$$dG(x, x_0, A, w) = A\frac{\frac{1}{w}}{\sqrt{e}}(x-x_0)e^{\frac{-(x-x_0)^2}{2\left(\frac{1}{w}\right)^2}} \tag{5}$$

The Ricker and Gaussian derivative wavelets may give ambiguous results in cases of closely spaced anomalies, causing difficulties in tracking the same anomaly in different logs.

3.2. Correlation of Anomalies Between Logs

We construct a symmetric correlation matrix that compares every Gaussian wavelet F_j with every other wavelet F_k (equation (6)).

$$p_{jk} = \frac{c_{jk}}{\sqrt{c_{jj}c_{kk}}} \tag{6}$$

where $c_{jk} = \sum F_{ji}F_{ki}$. Each element p_{jk} is a Pearson correlation coefficient. The closer the value is to 0, the lesser the similarity between the two compared features. Perfectly correlated wavelets have a correlation value of 1.

4. Results

We identify 192 anomalous features in our data set. We selected for analysis Gaussian wavelets that were significantly correlated (individual correlation coefficients >0.9) between four or more logs in the shallow part of the hole (< 550 m), and three or more in the deeper part (>550 m), where fewer logs had been acquired. This reduced the total number of anomalies into distinct depth intervals and removed random noise. The parameters of these anomalies are summarized in Figure 7. The width (width containing 95% of the area of the anomaly, where parameter w is ~25% of this width) of wavelets is of order 5–20 m, and larger for approximately a quarter of the wavelets (Figure 7). Most anomalies have amplitudes within $\pm 0.5^{\circ}$C (Figure 8). Below we refer to the anomalies with amplitudes $\geq 0.5^{\circ}$C as "major anomalies."

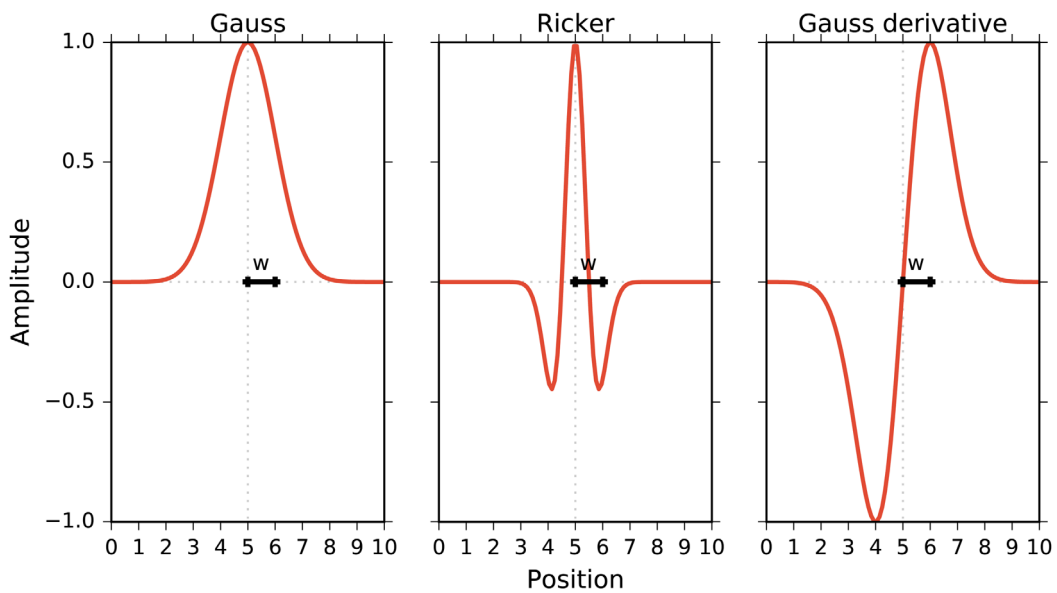

Figure 6. Gaussian, Ricker, and Gaussian derivative wavelets with the same parameters ([position, amplitude, width]; here [5,1,1]). The Gaussian wavelet was used for our analysis.

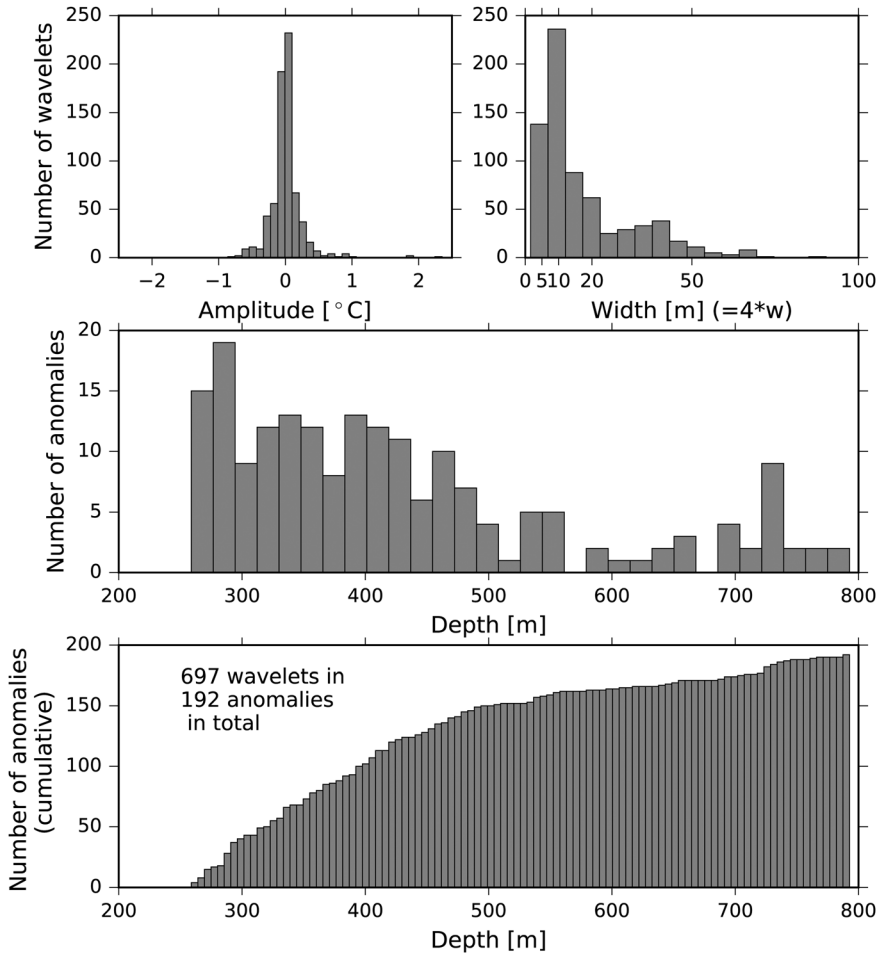

Figure 7. Histograms of the widths, amplitudes, and depths of the most correlating wavelets (across 4 or more logs, 3 below 550 m) and cumulative histogram of depth of thus identified anomalies. The lower number of wavelets below 500 m does not necessarily mean a lower number of fractures in the formation, but more likely represents the lower number of observations. Whereas the interval above 550 m is covered by 15 logs, it is likely that all major features causing anomalies, such as fractures, have been detected. The bottom part of the hole, which is only covered by four logs, may be underconstrained by observations.

5. Analysis and Discussion

Thermal disturbance in the borehole differs between each log, because each log was measured at a different time after circulation and drilling, and there were multiple drilling and/or mud circulation events. In the depth range investigated (below 260 m), the mud in DFDP-2B was cooler than the rock formation during all mud circulation events. We use fiber-optic temperature measurements acquired nearly a year after cessation of drilling (Sutherland et al., 2017) to estimate the equilibrium temperature before and after drilling.

We consider various possible reasons for the transient anomalies we observe in temperature logs: (1) downhole variations in thermal diffusivity; (2) fluid flow into or out of the borehole; and (3) fluid flow within formation that is hydraulically isolated from the borehole.

We present a simplified model at ~400 m depth, where initial temperature conditions and a boundary condition at 20 m radial distance are taken as 70°C, and the circulating fluid temperature is 30°C (constrained by mud temperature measurements, Figure 3a). The model built using FiPy (Guyer et al., 2009) has 4 days of mud circulation. The problem is solved using a two-step process. First, a constant temperature boundary condition is applied within the borehole to simulate drilling and circulation. In the second step, this boundary condition is removed, to simulate no activity in the borehole.

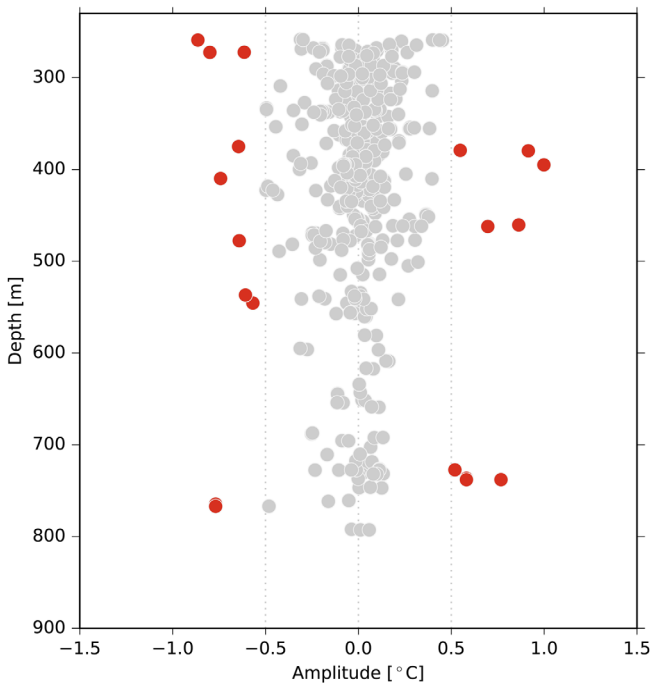

Figure 8. Amplitudes summed for each log at a given depth. The vertical lines at −0.5, 0, and 0.5 indicate the range of most anomalies (shown in grey). Major anomalies that have amplitudes outside this range are shown in red. No anomalies have been detected below 800 m because only a single log has been recorded in this depth range and, furthermore, at high logging speed.

In the first set of models, we assume no fluid flow and radial symmetry, and the temperature evolution surrounding the borehole is found by a 1-D solution (Figure 9). We next consider the effect of a range of values of thermal diffusivity, which may be caused by variable rock composition, again assuming no fluid flow and radial symmetry. The values considered are 1.0×10^{-6} to 2.0×10^{-6} m^2 s^{-1}, which is a reasonable range for the rock types encountered (Sutherland et al., 2017; Toy et al., 2017). Results are shown in Figure 10. Depending on the thermal diffusivity contrast, anomalies can be positive or negative. They reach a peak of 1–2°C during the first day after mud circulation stops, and then exponentially decay to <0.1°C within a week (Figure 10). A very thick vein of quartz with thermal diffusivity of 3.9×10^{-6} m^2 s^{-1} (Sundberg et al., 2009; Waples & Waples, 2004) could initially produce an anomaly of nearly 4°C and decay to 1°C after a week (Figure 10).

Mud level observations taken after circulation stopped (Figure 3) constrain the fluid budget of the borehole i.e., net inflow or outflow to the borehole from the rock. In general, the mud level dropped by 5–10 m during the first 2 days after circulation, and then slowly rose over the following week (Coussens, 2017; Townend et al., 2017). This is mostly explained by fluid pressure equilibration between the borehole and rock formation: dense mud percolates into the rock formation immediately after drilling; and then a phase of fluid production into the borehole may occur as mud density decreases with time due to settling of particles from the mud suspension.

The fluid budget of the borehole could also be satisfied if there was fluid loss in upper parts and fluid gain from the formation in lower parts (Coussens, 2017). However, unfiltered temperature data (Figure 4) do not contain concave-shaped zones that would indicate significant vertical flow in the hole (Kappelmeyer & Haenel, 1974). The amplitudes of the observed temperature anomalies are localized, persistent, and in the range ±1°C, which rules out the possibility of production or injection of significant volumes (>1 m^3) of fluid through a single fracture zone over sustained periods of time. However, small-scale localized injection of mud into the formation or production from the formation could partly explain individual anomalies.

We propose that the primary cause of multiple anomalies in temperature logs is related to the combination of a high temporary thermal gradient normal to the borehole (10s of °C on meter-scales, Figure 9) and a component of lateral fluid flow. We model the temperature evolution in 2-D, assuming fluid migration is occurring in the fractured rock mass in a thick planar zone normal to the borehole. We assume no flow into or out of the borehole, to simulate the case that drilling fluid effectively blocks inflow from all fractures close to the borehole wall (we do not include a radial flow component).

The heat flow equation (7) is:

$$\frac{\partial T}{\partial t} = \kappa_b \nabla \cdot \nabla T - \frac{C_f}{C_b} \vec{u_f} \cdot \nabla T \tag{7}$$

where κ_b is bulk thermal diffusivity, T is temperature, C_f and C_b are volumetric heat capacities of fluid and the bulk mixture (fluid and rock), respectively, $\vec{u_f}$ is the fluid Darcy velocity vector ("fluid flux"). The approximate thermal diffusivity of bulk rock at DFDP-2B is taken to be 1.5×10^{-6} m^2 s^{-1} (Sutherland et al., 2017).

Figure 11 shows that fluid flow within a plane normal to the borehole causes the drilling-related thermal anomaly to become asymmetric around the borehole, and then it is advected away from the borehole after mud circulation stops and the anomaly diffuses. High rates of fluid advection cause temperature within the borehole to rise more rapidly than might otherwise be expected: (1) high temperatures are located closer at the end of drilling, due to asymmetry induced by flow; and (2) the axis of the cool thermal anomaly is advected away from the borehole.

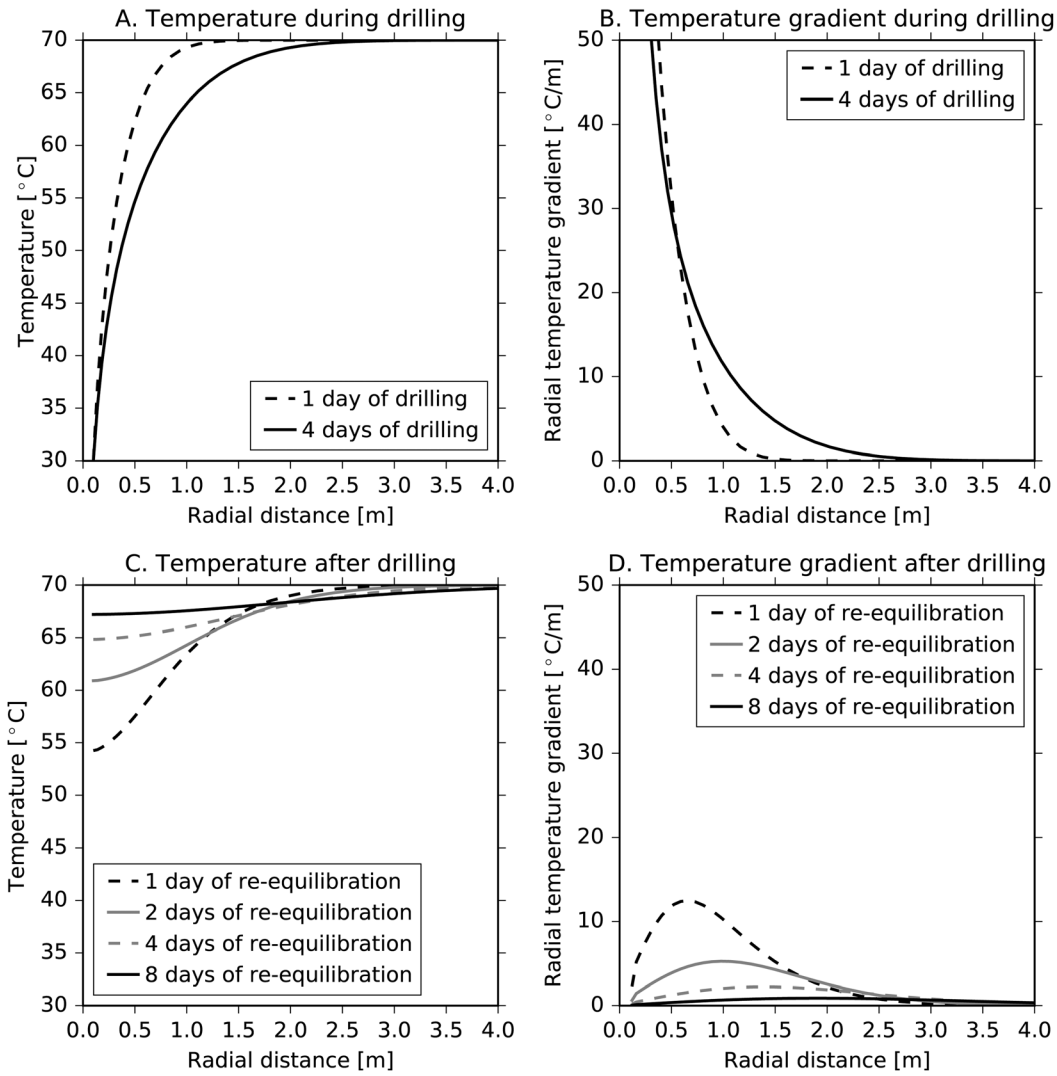

Figure 9. A 1-D radial diffusion model illustrating (a and b) a case of drilling and circulation, followed by (c and d) a period of re-equilibration with the surrounding rock mass. This is the radially-symmetric case with no fluid flux, $|\vec{u_f}|=0$.

The borehole-normal length scales of interest are small (~2 m) compared to the borehole-parallel observed widths of anomalies (Figure 7), so our 2-D approximation is reasonable. For fluid flux values higher than 1×10^{-6} m s^{-1}, the anomaly is much greater during the first few days after drilling, and decays toward a value similar to observations within a couple of weeks (Figure 12). For fluid flux values in the range 1×10^{-7}–1×10^{-6} m s^{-1}, the temperature anomaly is established within a few hours of cessation of drilling and remains relatively constant in the range of 0.5°C–1.5°C, which is a good match to observed values (Figure 8 and 13).

Numerical models that simulate the regional-scale temperature field (Sutherland et al., 2017) are consistent with the equilibrium temperature profile and predict upward fluid flux in the Whataroa Valley near DFDP-2B of order 1×10^{-9} to 1×10^{-8} m s^{-1} averaged over the entire hanging-wall (Sutherland et al., 2017). It is likely that this flow is concentrated in the "outer damage zone" (Townend et al., 2017), which is intersected by the borehole. Our estimates of borehole-normal flux of 1×10^{-7} to 1×10^{-6} m s^{-1} imply that regional flow is restricted to fractured zones that represent only ~1% of the rock mass by volume, though the DFDP-2B borehole may contain a higher-than-average proportion of fractured zones due to its close proximity to the Alpine Fault. The "borehole-normal" flux here is the borehole-normal component of the total flux parallel to fracture plains intersecting the inclined borehole at various angles, and contributing to the overall upward flow on the regional scale. Due to a complex 3-D flow pattern caused by the relief and the

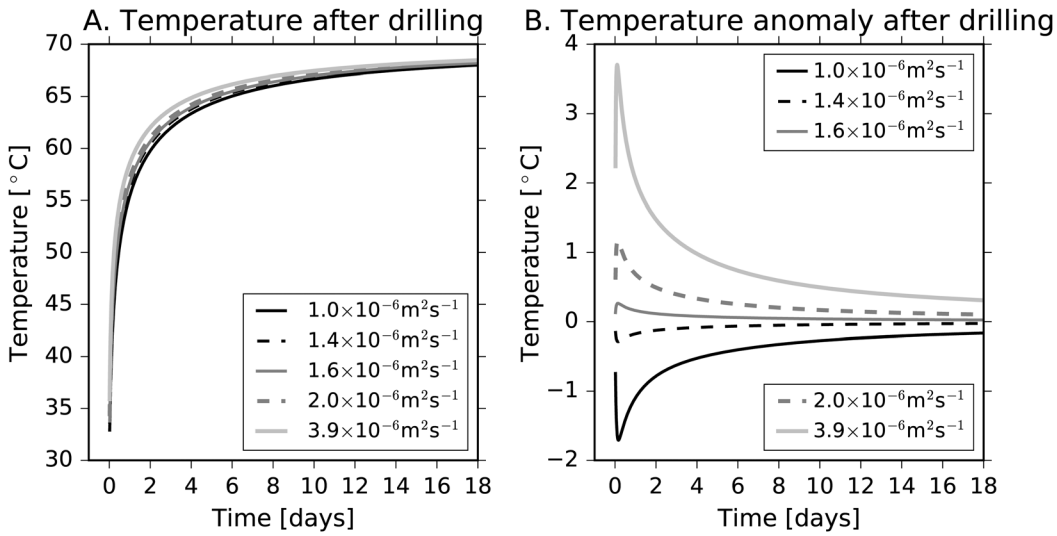

Figure 10. Temperature as a function of time for a radial diffusion model with different thermal diffusivities, as compared to a reference model of 1.5×10^{-6} m^2 s^{-1}. The time refers to cessation of mud circulation in the borehole.

dip of tectonic structures, the direction in which flux is quantified must be specified. Here, we only refer to close surroundings of the borehole, in which all flow can be approximated as lateral.

Temperature anomalies with highest amplitudes are mostly observed within the first day after circulation, but anomalies with amplitudes up to 50–70% of these peak values persist up to 15 days after drilling (Figure 13). A small number of outliers with high amplitude may reflect natural or logging-induced changes in the borehole, such as partial borehole wall collapse or bentonite mud washed out from fractures. The high amplitudes of anomalies during the first day are consistent with diffusive processes and may be related to downhole contrasts in thermal or hydraulic diffusivity. The rapidly dropping mud level during the first day after mud circulation attests to radial flow being a contributing factor to this group of anomalies. We interpret anomalies that do not decay significantly during the first couple of days after mud circulation ceases to reflect background fluid flow within fractured zones of the surrounding rock mass that interact with high lateral temperature gradients induced by drilling (Figure 13).

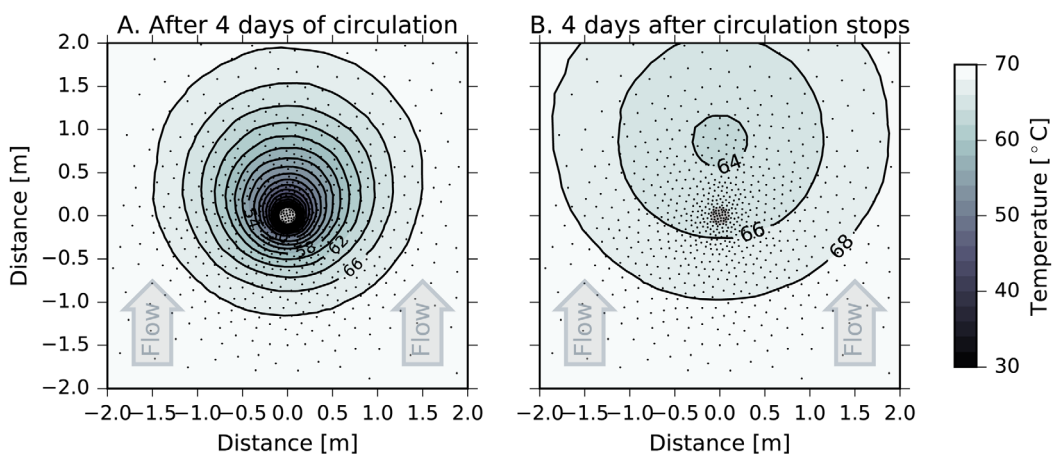

Figure 11. The 2-D radial model with the borehole in the center at coordinates (0,0). Black dots are mesh nodes of the model's mesh. We apply Darcy velocity of 1×10^{-6} m s^{-1} toward the top of the plot (indicated by arrows). (a) Conditions after 4 days of mud circulation in the borehole (end of step 1). (b) Conditions after a further 4 days of equilibration with no mud circulation in the borehole (end of step 2). The process of thermal disturbance and re-equilibration is shown in the supporting information videos.

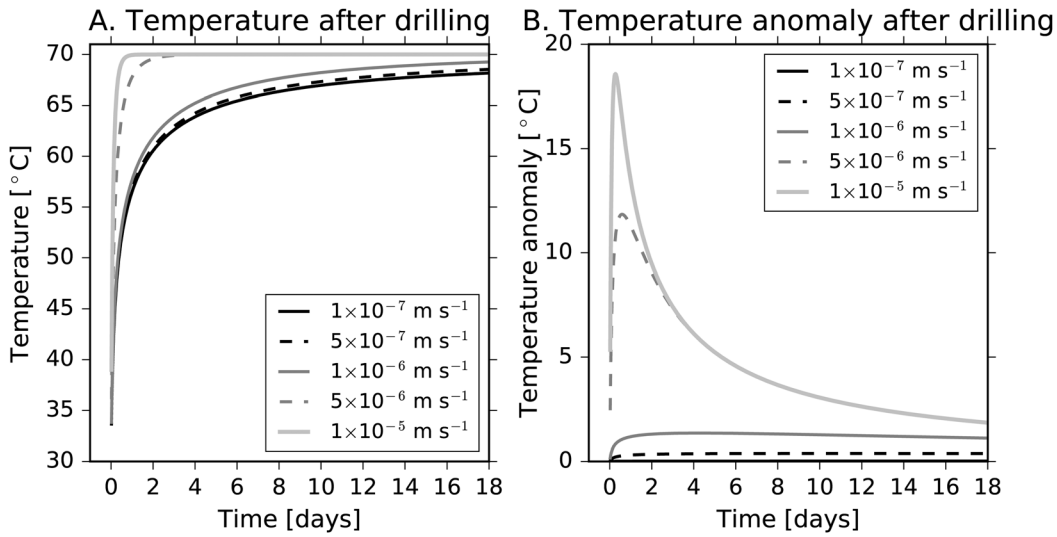

Figure 12. Temperature as a function of time for a radial diffusion model with different advective Darcy velocities, as compared to a reference model with no advective term. The time refers to cessation of mud circulation in the borehole.

There exists bias in our observations, because deeper portions of the borehole (below 550 m) were logged only twice and breaks in drilling lasted only a few days. Therefore, we cannot fit a particular model to each individual anomaly with confidence, but the overall pattern of anomaly amplitudes with time (Figure 13) clearly shows that multiple anomalies persist for longer than can be explained by diffusive processes alone.

The procedure we use to filter temperature logs produces an approximately equal number of positive and negative anomalies, but the baseline definition of anomaly amplitudes is arbitrary. Our models of background fluid flow predict persistent temperature anomalies with positive amplitudes in fractured zones. For persistent anomalies, the appropriate baseline definition is the minimum temperature in adjacent parts of the log.

Some of the temperature anomalies with largest amplitude (Figure 8) coincide with anomalies in other observations, such as changes in geothermal gradient of the equilibrated temperature profile, increases of resistivity and natural gamma activity, a zone of drilling mud loss at ∼730 m depth (Sutherland et al., 2017; Townend et al., 2017), or an increase in sonic amplitude and natural gamma activity at ∼470 m depth

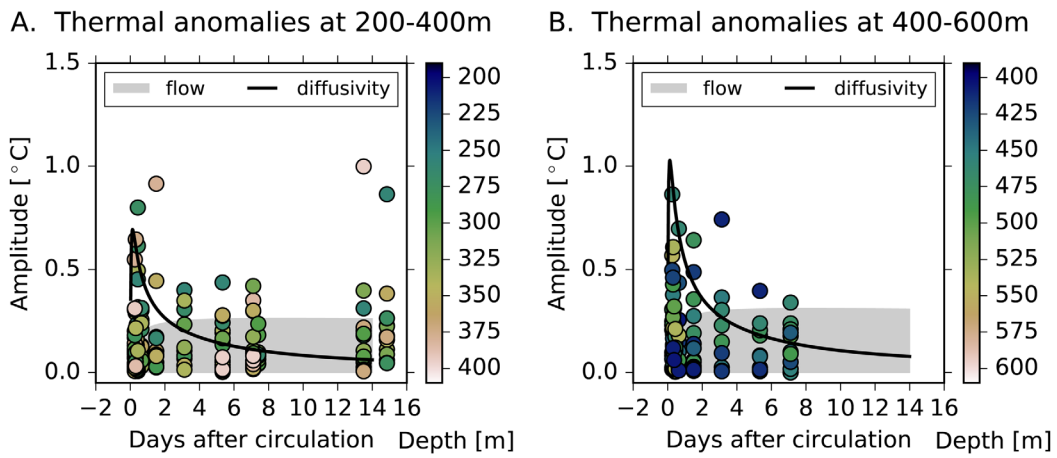

Figure 13. We compare the absolute values of amplitudes observed at different times after the last circulation in two depth regions and compare them with models of fluid flux (5×10^{-7} m s^{-1}) and thermal diffusivity contrast of 0.3×10^{-6} m^2 s^{-1} at the center of this depth range. Only two runs (R45 and R49) cover the interval below 600 m depth and these were performed within the first day after circulation. Their decay rate is, thus, unknown and we do not show them here.

(Townend et al., 2017). We do not observe temperature anomalies between 550 and 700 m, which corresponds to a depth range of high gamma activity and sonic amplitude (Townend et al., 2017) and low image quality of BHTV logs (Massiot, 2017).

6. Conclusions

We use a discrete wavelet method to identify nearly two hundred anomalies in 16 temperature logs in the DFDP-2B borehole. Anomalies generally have amplitudes $<1^{\circ}$C relative to the long-wavelength temperature value estimated using a sixth-order polynomial. Anomalies typically have downhole widths <20 m. The largest values are found in the first day after mud circulation stops, but some anomalies persist with similar values for up to 15 days.

High amplitude temperature anomalies during the first day after mud circulation can be explained by downhole variations in thermal and hydraulic diffusivity, but we interpret persistent anomalies as being caused by background fluid flow in the formation. Our models show that diffusive processes are dominant during the first few days of thermal and hydrogeological re-equilibration after drilling, and advective processes become dominant on the timescale of weeks. Anomalies associated with diffusive processes allow us to resolve layers of contrasting thermal or/and hydraulic properties in the rock formation. The persistent temperature anomalies are produced by the combination of extreme lateral thermal gradients induced by drilling and mud circulation process (diffusive cooling caused by 30–60°C difference over a few meters), and fluid flux of order 10^{-7} to 10^{-6} m s^{-1} within the rock mass that advects heat subparallel to the temperature gradient vector. These fluxes are 2–3 orders of magnitude higher than reported from Swiss Alps (Bodri & Rybach, 1998) and 1–2 orders of magnitude higher than in the South German Molasse Basin (Zschocke et al., 2005). Localized zones of rapid fluid flow in otherwise impermeable rock have also been observed in the Himalayas (Whipp & Ehlers, 2007). However, the fluxes that we observe are unusual even for a tectonically active mountainous region on the global scale. And yet, fluxes in the DFDP-2B clearly do not represent the highest values to be encountered in the Southern Alps. Natural hot springs such as Copland exhibit fluxes of the order of 10^{-1} m s^{-1} (Cox et al., 2014).

DFDP-2B is unique among scientific boreholes in that it discovered a geothermal gradient that is extremely high for a nonvolcanic region. The high temperatures at shallow depth can be explained by a combination of rock advection bringing heat from depth and fluid advection moving heat from mountains to valleys (Sutherland et al., 2017). The regional fluid flux can be estimated from simplified models and is clearly influenced by a permeable outer damage none of an active fault (Townend et al., 2017). However, permeability is concentrated along discrete fractured zones. We have been able to use the temperature logs to locate these fractured zones and estimate the order of magnitude of fluid flux that is concentrated within these zones.

Acknowledgments
We thank Jehanne Paris, Gilles Henry, and Olivier Nitch from CNRS Montpellier for providing their logging equipment and expertise on site and Philippe Pezard for organizing their expedition. We gratefully acknowledge the support from Alex Pyne, Ray Marx, Tony Kingan, and the Webster Drilling that enabled us to measure so many logs. We sincerely thank Steve Ingebritsen for detailed and very helpful comments on this manuscript. Funding for the Deep Fault Drilling Project was provided by the International Continental Scientific Drilling Program (ICDP), Marsden Fund of the Royal Society of New Zealand, GNS Science, Victoria University of Wellington, University of Otago, NZ Ministry for Business Innovation and Employment, and NERC grants NE/J022128/1 and NE/J024449/1. Janku-Capova's PhD project is a part of DFDP and is funded by Earthquake Commission Student grant E2568/3185 and co-supported by Victoria University of Wellington funds. Postdrilling cooperation of the Wireline Logging Subteam was funded under the terms of the Dumont d'Urville NZ-France Science & Technology Support Programme. Numerical models were created using the FiPy module in Python. Relevant data (displayed in Figures 2–4) are provided as supporting information. The current code is under further development, but available upon request from R. Sutherland (Victoria University of Wellington). Further details regarding data acquisition are available in the DFDP-2 completion report (Sutherland et al., 2015), more data from DFDP are available from the ICDP website under Australia and New Zealand projects (Alpine Fault).

References

Adams, J. (1980). Contemporary uplift and erosion of the Southern Alps, New Zealand: Summary. *Geological Society of America Bulletin*, *91*(1), 2–4. https://doi.org/10.1130/0016-7606(1980)91.

Allis, R. G., & Shi, Y. (1995). New insights to temperature and pressure beneath the central Southern Alps, New Zealand. *New Zealand Journal of Geology and Geophysics*, *38*(4), 585–592. https://doi.org/10.1080/00288306.1995.9514687

Barton, C., Zoback, M., & Moos, D. (1995). Fluid-flow along potentially active faults in crystalline rock. *Geology*, *23*(8), 683–686. https://doi.org/10.1130/0091-7613(1995)0232.3.CO;2

Beavan, J., Denys, P., Denham, M., Hager, B., Herring, T., & Molnar, P. (2010). Distribution of present-day vertical deformation across the Southern Alps, New Zealand, from 10 years of GPS data. *Geophysical Research Letters*, *37*, L16305. https://doi.org/10.1029/2010GL044165

Bodri, B., & Rybach, L. (1998). Influence of topographically driven convection on heat flow in the Swiss Alps: A model study. *Tectonophysics*, *291*(1–4), 19–27.

Bredehoeft, J. D., & Papaopulos, I. S. (1965). Rates of vertical groundwater movement estimated from the Earth's thermal profile. *Water Resources Research*, *1*(2), 325–328. https://doi.org/10.1029/WR001i002p00325

Clauser, C., Giese, P., Huenges, E., Kohl, T., Lehmann, H., Rybach, L., et al. (1997). The thermal regime of the crystalline continental crust: Implications from the KTB. *Journal of Geophysical Research*, *102*(B8), 18417–18441.

Coussens, J. (2017). *Fluid flow in an active orogenic mountain belt: the Southern Alps, New Zealand* (PhD thesis). Southampton, UK: University of Southampton.

Cox, S. C., Menzies, C. D., Sutherland, R., Denys, P. H., Chamberlain, C., & Teagle, D. A H. (2014). Changes in hot spring temperature and hydrogeology of the Alpine Fault hanging wall, New Zealand, induced by distal South Island earthquakes. *Geofluids*, *15*, 216–239, https://doi.org/10.1111/gfl.12093

Cox, S. C., & Sutherland, R. (2007). Regional geological framework of South Island, New Zealand, and its significance for understanding the active plate boundary. In D. Okaya, T. Stern, & F. Davey (Eds.), *A continental plate boundary: Tectonics at South Island, New Zealand, Geophysical monograph series* (Vol. 175, pp. 19–46). Washington, DC: American Geophysical Union. https://doi.org/10.1029/175GM03 doi:10.1029/175GM03, Plate 10.1029/175GM03, Plate.

Drury, M. J. (1989). Fluid flow in crystalline crust: Detecting fractures by temperature logs. In A. E. Beck, G. Garven, & L. Stegena (Eds.), *Hydrogeological regimes and their subsurface thermal effects* (Vol. 47, pp. 129–135). Washington, DC: American Geophysical Union. https://doi.org/10.1029/GM047p0129

Drury, M. J., & Jessop, A. (1982). The effect of a fluid-filled fracture on the temperature profile in a borehole. *Geothermics*, *11*(3), 145–152. https://doi.org/10.1016/0375-6505(82)90023-2

Drury, M. J., Jessop, A., & Lewis, T. (1984). The detection of groundwater flow by precise temperature measurements in boreholes. *Geothermics*, *13*(3), 163–174. https://doi.org/10.1016/0375-6505(84)90013-0

Ge, S. (1998). Estimation of groundwater velocity in localized fracture zones from well temperature profiles. *Journal of Volcanology and Geothermal Research*, *84*(1–2), 93–101. https://doi.org/10.1016/S0377-0273(98)00032-8

Guyer, J. E., Wheeler, D., & Warren, J. A. (2009). FiPy: Partial Differential Equations with Python. *Computing in Science & Engineering*, *11*(3), 6–15. https://doi.org/10.1109/MCSE.2009.52

Hickman, S., Sibson, R., & Bruhn, R. (1995). Introduction to special section: Mechanical involvement of fluids in faulting. *Journal of Geophysical Research*, *100*(B7), 12831–12812,840. https://doi.org/10.1029/95JB01121

Jobmann, M., & Clauser, C. (1994). Heat advection versus conduction at the KTB: Possible reasons for vertical variations in heat-flow density. *Geophysical Journal International*, *119*(1), 44–68. https://doi.org/10.1111/j.1365-246X.1994.tb00912.x

Kappelmeyer, O., & Haenel, R. (1974). *Geothermics with special reference to application* (Vol. 1, 238 pp.). Stuttgart, Germany: Gebrüder Borntraeger.

Kohl, T., & Rybach, L. (1996). Thermal and hydraulic aspects of the KTB drill site. *Geophysical Journal International*, *124*(3), 756–772. https://doi.org/10.1111/j.1365-246X.1996.tb05636.x

Koons, P. (1987). Some thermal and mechanical consequences of rapid uplift: An example from the Southern Alps, New Zealand. *Earth and Planetary Science Letters*, *86*(2–4), 307–319. https://doi.org/10.1016/0012-821X(87)90228-7

Lachenbruch, A. H., & Brewer, M. C. (1959). Dissipation of the temperature effect of drilling a well in Arctic Alaska. *United States Geological Survey Bulletin*, *1083*, 73–109.

Little, T. A., Cox, S., Vry, J. K., & Batt, G. (2005). Variations in exhumation level and uplift rate along the oblique-slip Alpine fault, central Southern Alps, New Zealand. *Geological Society of America Bulletin*, *117*(5), 707–723. https://doi.org/10.1130/B25500.1

Massiot, C. (2015). *Structural analysis of acoustic image logs from the DFDP-2B borehole, central Alpine Fault*. Paper presented at Poster presentation at Annual Conference of the Geoscience Society of New Zealand, 24–27 November, Wellington, New Zealand.

Massiot, C. (2017). *Fracture system characterization and implications for fluid flow in volcanic and metamorphic rocks* (PhD thesis). Wellington, New Zealand: Victoria University of Wellington.

Menzies, C. D., Teagle, D. A. H., Craw, D., Cox, S. C., Boyce, A. J., Barrie, C. D., et al. (2014). Incursion of meteoric waters into the ductile regime in an active orogen. *Earth and Planetary Science Letters*, *399*, 1–13. https://doi.org/10.1016/j.epsl.2014.04.046

Michalski, A. (1989). Application of temperature and electrical-conductivity logging in ground water monitoring. *Ground Water Monitoring & Remediation*, *9*(3), 112–118. https://doi.org/10.1111/j.1745-6592.1989.tb01158.x

Norris, R. J., & Cooper, A. F. (1997). Erosional control on the structural evolution of a transpressional thrust complex on the Alpine fault, New Zealand. *Journal of Structural Geology*, *19*(10), 1323–1342. https://doi.org/10.1016/S0191-8141(97)00036-9

Norris, R. J., & Cooper, A. F. (2001). Late Quaternary slip rates and slip partitioning on the Alpine Fault, New Zealand. *Journal of Structural Geology*, *23*(2–3), 507–520. https://doi.org/10.1016/S0191-8141(00)00122-X

Norris, R. J., & Cooper, A. F. (2007). The alpine Fault, New Zealand: Surface geology and field relationships. In D. Okaya, T. Stern, & F. Davey (Eds.), *A continental plate boundary: Tectonics at south Island, New Zealand, Geophysical monograph series* (Vol. 175, pp. 157–175). Washington, DC: American Geophysical Union. https://doi.org/10.1029/175GM09/175GM09

Popov, Y. A., Pevzner, S. L., Pimenov, V. P., & Romushkevich, R. A. (1999). New geothermal data from the Kola superdeep well SG-3. *Tectonophysics*, *306*(3–4), 345–366. https://doi.org/10.1016/S0040-1951(99)00065-7

Reiter, M. (2001). Using precision temperature logs to estimate horizontal and vertical groundwater flow components. *Water Resources Research*, *37*(3), 663–674. https://doi.org/10.1029/2000WR900302

Remaud, L. (2015). *Study of the damage zone around the Alpine Fault, New Zealand, from borehole data of the Deep Fault Drilling Project (stage 2)* (Master's thesis). Grenoble, France: Université Joseph Fourier.

Saar, M. O. (2011). Review: Geothermal heat as a tracer of large-scale groundwater flow and as a means to determine permeability fields. *Hydrogeology Journal*, *19*(1), 31–52. https://doi.org/10.1007/s10040-010-0657-2

Sundberg, J., Back, P.-E., Ericsson, L. O., & Wrafter, J. (2009). Estimation of thermal conductivity and its spatial variability in igneous rocks from in situ density logging. *International Journal of Rock Mechanics and Mining Sciences*, *46*(6), 1023–1028. https://doi.org/10.1016/j.ijrmms.2009.01.010

Sutherland, R., Berryman, K., & Norris, R. (2006). Quaternary slip rate and geomorphology of the Alpine fault: Implications for kinematics and seismic hazard in southwest New Zealand. *Geological Society of America Bulletin*, *118*(3–4), 464–474. https://doi.org/10.1130/b25627.1

Sutherland, R., Toy, V. G., Townend, J., Cox, S. C., Eccles, J. D., Faulkner, D. R., et al. (2012). Drilling reveals fluid control on architecture and rupture of the Alpine fault, New Zealand. *Geology*, *40*(12), 1143–1146. https://doi.org/10.1130/g33614.1

Sutherland, R., J., Townend, V., Toy, M., Allen, L., Baratin, N., Barth, L., et al. (2015). *Deep Fault Drilling Project (DFDP), Alpine fault boreholes DFDP-2A and DFDP-2B technical completion report* (Tech. Rep. 50). Lower Hutt, New Zealand: Institute of Geological and Nuclear Sciences Limited.

Sutherland, R., Townend, J., Toy, V. G., & Upton, P. and DFDP-2B Science Team (2017). Extreme hydrothermal conditions at an active plate-bounding fault. *Nature*, *546*, 137–140. https://doi.org/10.1038/nature22355

Townend, J., Sutherland, R., & Toy, V. (2009). Deep fault drilling project, Alpine Fault, New Zealand. *Scientific Drilling*, *8*, 75–82. https://doi.org/10.2204/iodp.sd.8.12.2009

Townend, J., Sutherland, R., Toy, V. G., Doan, M.-L., Celerier, B., Massiot, M., et al. (2017). Petrophysical, geochemical, and hydrologic evidence for extensive fracture-mediated fluid and heat transport in the Alpine Fault's hanging-wall damage zone. *Geochemistry Geophysics Geosystems*, *18*, 4709–4732. https://doi.org/10.1002/2017GC007202

Toy, V. G., Boulton, C. J., Sutherland, R., Townend, J., Norris, R. J., Little, T. A., et al. (2015). Fault rock lithologies and architecture of the central Alpine fault, New Zealand, revealed by DFDP-1 drilling. *Lithosphere*, *7*(2), 155–173. https://doi.org/10.1130/L395.1

Toy, V. G., Sutherland, R., Townend, J., Allen, M. J., Becroft, L., Boles, A., et al (2017). Bedrock geology of DFDP-2B, central Alpine Fault, New Zealand. *New Zealand Journal of Geology and Geophysics*, *64*, 497–518. https://doi.org/10.1080/00288306.2017.1375533

Upton, P., Koons, P. O., & Chamberlain, C. P. (1995). Penetration of deformation driven meteoric water into ductile rocks: Isotopic and model observations from the Southern Alps, New Zealand. *New Zealand Journal of Geology and Geophysics*, *38*(4), 535–543. https://doi.org/10.1080/00288306.1995.9514680

Upton, P., & Sutherland, R. (2014). High permeability and low temperature correlates with proximity to brittle failure within mountains at an active tectonic boundary, Manapouri tunnel, Fiordland, New Zealand. *Earth and Planetary Science Letters*, *389*, 176–187. https://doi.org/10.1016/j.epsl.2013.12.032

Vidal, J., Genter, A., & Schmittbuhl, J. (2016). Pre- and post-stimulation characterization of geothermal well GRT-1, Rittershoffen, France: Insights from acoustic image logs of hard fractured rock. *Geophysical Journal International*, *206*(2), 845–860. https://doi.org/10.1093/gji/ggw181

Waples, D. W., & Waples, J. S. (2004). A review and evaluation of specific heat capacities of rocks, minerals, and subsurface fluids. Part 1: Minerals and nonporous rocks. *Natural Resources Research*, *13*(2), 97–122. https://doi.org/10.1023/B:NARR.0000032647.41046.e7

Whipp, D. M., & Ehlers, T. A. (2007). Influence of groundwater flow on thermochronometer-derived exhumation rates in the central Nepalese Himalaya. *Geology*, *35*(9), 851–854. https://doi.org/10.1130/G23788A.1

Ziagos, J. P., & Blackwell, D. D. (1986). A model for the transient temperature effects of horizontal fluid flow in geothermal systems. *Journal of Volcanology and Geothermal Research*, *27*(3–4), 371–397. https://doi.org/10.1016/0377-0273(86)90021-1

Zschocke, A., Rath, V., Grissemann, C., & Clauser, C. (2005). Estimating Darcy flow velocities from correlated anomalies in temperature logs. *Journal of Geophysics and Engineering*, *2*(4), 332–342. https://doi.org/10.1088/1742-2132/2/4/S06